




Impacts of Mineralogy on Petrophysical Properties

Maira C. O. Lima¹ · Elizabeth M. Pontedeiro^{1,3} · Mateus G. Ramirez² · Julia Favoreto⁴ · Héllisson N. dos Santos⁴ · Martinus Th. van Genuchten^{3,5} · Leonardo Borghi⁴ · Paulo Couto¹ · Amir Raouf³ 

Received: 17 February 2022 / Accepted: 7 July 2022 / Published online: 26 August 2022
© The Author(s) 2022

Abstract

Because of their extreme heterogeneity at multiple scales, carbonate rocks present a great challenge for studying and managing oil reservoirs. Depositional processes and diagenetic alterations of carbonates may have produced very complex pore structures and, consequently, variable fluid storage and flow properties of hydrocarbon reservoirs. To understand the impact of mineralogy on the pore system, we analyzed four carbonate rock samples (coquinas) from the Morro do Chaves Formation in Brazil. For this study, we used thin sections and XRD for their mineralogical characterization, together with routine core analysis, NMR, MICP and microCT for the petrophysical characterizations. The samples revealed very similar porosity values but considerably different permeabilities. Samples with a relatively high quartz content (terrigenous material) generally had lower permeabilities, mostly caused by more mineral fragmentation. Samples with little or no quartz in turn exhibited high permeabilities due to less fragmentation and more diagenetic actions (e.g., dissolution of shells). Results confirm that carbonate minerals are very susceptible to diagenesis, leading to modifications in their pore body and pore throat sizes, and creating pores classified as moldic and vug pores, or even clogging them. For one of the samples, we acquired detailed pore skeleton information based on microCT images to obtain a more complete understanding of its structural characteristics.

Keywords Carbonate rocks · Heterogeneity · Pore scale · Coquinas · Petrophysical properties · Permeability

✉ Amir Raouf
A.Raouf@uu.nl

¹ Department of Civil Engineering, COPPE, Federal University of Rio de Janeiro, Rio de Janeiro, Brazil

² Department of Mechanical Engineering, COPPE, Federal University of Rio de Janeiro, Rio de Janeiro, Brazil

³ Department of Earth Sciences, Utrecht University, Utrecht, The Netherlands

⁴ Department of Geology, LAGESED, Federal University of Rio de Janeiro, Rio de Janeiro, Brazil

⁵ Department of Nuclear Engineering, COPPE, Federal University of Rio de Janeiro, Rio de Janeiro, Brazil

1 Introduction

Many carbonate rocks form major hydrocarbon reservoirs. Even though they represent only about 20% of all sedimentary rocks, they contain more than 60% of global conventional hydrocarbon resources (Ahr 2008; Jia 2012). Carbonate rocks typically are very heterogeneous at multiple scales, leading to complex pore structures with unique fluid retention and flow properties (Lønøy 2006; Sun et al. 2017). Because of their geologic complexity, hydrocarbon reservoirs have become a widely discussed frontier in science and engineering (Ceraldi and Green 2016; Herlinger et al. 2017), including those of the Brazilian pre-salt. Pre-salt carbonate rocks in the South Atlantic contain very large hydrocarbon reservoirs (Mohriak 2014). They were deposited in lacustrine environments, associated with the development of rift and sag basins, during the separation of the Gondwana supercontinent and the opening of the South Atlantic Ocean in the Upper Jurassic/Lower Cretaceous (Cainelli and Mohriak 1999; Mohriak et al. 2008). According to Favoreto et al. (2021), bioclastic accumulations in Brazil (e.g., the Itapema, Coqueiros and Morro do Chaves Formations in the Santos, Campos and Sergipe-Alagoas basins, respectively) are similar to those deposited along the West Bank of Africa (e.g., the Toca and Marnes Noires Formations in the Congo and Cabinda basins). With these discoveries, lacustrine carbonates have become a major focus of hydrocarbon recovery efforts in deep waters (Herlinger et al. 2017).

The Morro do Chaves Formation is a hybrid deposit, composed of coquinas and siliciclastic sediments represented by shales and sandstones (Azambuja and Arienti 1998; Campos Neto et al. 2007; Rigueti et al. 2020). Even though coquinas from the Coqueiros and Itapema Formations (pre-salt Brazilian reservoirs) formed mainly by bivalves and ostracods (Mizuno et al. 2018; Lima and De Ros 2019; Leite et al. 2020; Olivito and Souza 2020), they had relatively little siliciclastic input but far more contributions from carbonate (e.g., ooids, oncoids, fragments of shrubs) and stevensitic grains (mud, stevensitic ooids) (Chinelatto et al. 2020) as compared to the Morro do Chaves Formations (Tavares et al. 2015; Porto-Barros et al. 2020). Accurate characterization of the petrophysical properties of coquinas is challenging because of multiscale geologic heterogeneities caused by the different sedimentation processes (Carvalho et al. 2000; Thompson et al. 2015) and subsequent diagenetic alterations (Tavares et al. 2015; Corbett et al. 2016). Understanding the main factors that control the petrophysical characteristics of coquinas can assist in the exploration of the pre-salt oil reserves (Chinelatto et al. 2020).

The main petrophysical properties of rocks, notably porosity and permeability, initially were controlled by environmental conditions during sediment deposition, with subsequent modifications through diagenetic actions (Tavares et al. 2015). Factors such as grain size and the type and stage of compaction directly affect porosity and, consequently, permeability. Permeability stands out as one of the most important petrophysical parameters reflecting the percolation flow capacity of reservoir fluids (Sun et al. 2017; Wang et al. 2020a, b). Although permeability is a well-established property when considering relatively uniform porous media, its precise dependence on complex geometries and topologies such as those of carbonate rocks is still not well understood (Basan et al. 1997; Zhao et al. 2022).

Two of the most basic reservoir performance characteristics are the overall pore size and pore throats distributions, which control the fluid storage capacity and the ability to conduct fluid out of the pore space (Zeng et al. 2017). These distributions can be defined using nuclear magnetic resonance (NMR) and mercury intrusion by capillary pressure (MICP) experiments, respectively. NMR allows the pore space to be evaluated indirectly through the excitation of nuclear spins, mainly ^1H contained in the saturating fluid molecules,

leading to estimates of both porosity and the pore size distribution (Souza et al. 2013). MICP, on the other hand, involves the injection of mercury as a non-wetting phase in the pore system and uses the gradual increase in mercury injection pressure to overcome capillary pressures associated with pore throats. The resulting MICP curves reflect mostly the pore throat sizes of a rock (Tian et al. 2018).

Previous studies of coquinas from the Morro do Chaves Formation focused on their petrophysical properties as obtained using routine core analysis with NMR, MICP and pore networking modeling of the permeability, as well as using microCT images (Corbett et al. 2016, 2017; Luna et al. 2016; Hoerlle et al. 2018; Lima et al. 2020), especially in view of their heterogeneity. Chinelatto et al. (2020) described very similar coquinas from the Brazilian offshore Itapema Formation. They associated the observed heterogeneity with the geological characteristics, showing that porosity and permeability were controlled by the texture characteristics of the coquinas as revealed by routine core analyses and high-resolution 3D images.

As noted by Zhao et al. (2016) and others, factors affecting porosity and permeability include grain size, sorting, type and degree of compaction, and amount and location of diagenetic cements. This multitude of factors makes it difficult to interpret the petrophysical properties of rocks and correlating the effects of mineralogy to the fluid flow properties (Gao and Li 2016). Mehmani et al. (2020) mentioned that pore-scale modeling, based on microCT images, allows direct identification and quantification of parameters related to pore structure and fluid properties for linking the fluid rock flow properties with geological information and establishing reliable rock classes. With this approach, modeling can optimize the number of experimental measurements needed for relating petrophysical rock types with depositional classifications (Chandra et al. 2015; Skalinski and Kenter 2015). To better address these issues, we characterized in our study the mineralogy, pore morphology, pore size distribution, porosity and permeability using various experimental techniques such as X-ray diffraction (XRD), thin sections, computerized microtomography (microCT), routine core analysis (RCAL), capillary pressure mercury injection (MICP) and nuclear magnetic resonance (NMR), along with detailed pore network modeling. By doing so, this study provides a more accurate and fundamental understanding of how rock flow properties are influenced by the petrophysical characteristics of a sample.

2 Geological Setting

The Sergipe-Alagoas Basin, located in northeastern Brazil, comprises a narrow strip between 20 and 50 km wide and 350 km long. The basin occupies an area of approximately 32,760 km², covering parts of Sergipe and Alagoas states as well as a small portion of Pernambuco, with one-third emerging and two-thirds being submerged up to a 3000 m isobath (ANP 2018). The basin is bounded to the north by Maragogi High, and to the south by the Vaza-Barris Fault System which separates from the Pernambuco-Paraíba and Jacuípe basins (Azambuja and Arienti 1998).

The Sergipe-Alagoas Basin exhibits the most complete sedimentary succession of all basins located along the eastern Brazilian coast. Its sedimentary record shows five different tectonic-stratigraphic phases: Paleozoic, the Pre-Rift phase, the Rift phase, the Post-Rift phase, and the Drift phase (Campos Neto et al. 2007). According to Favoreto et al. (2021), the Morro do Chaves Formation is deposited in a rift lake marked by oscillations in salinity related to climate fluctuations. The formation is defined by a carbonate succession (Jiquié

age), having a thickness varying between 50 and 350 m. It was formed by the accumulation of coquinas and mudstones from lacustrine environments, interspersed with siliciclastic rocks from the Coqueiro Seco Formation and fluvial-deltaic lacustrine mudstones and sandstones from the Penedo Formation (Azambuja and Arienti 1998; Campos Neto et al. 2007). The formation is composed of fan-delta facies associated with a fault edge to the northeast of the basin, presenting conglomerates reworked by waves, sandstones interspersed with bivalves, and thick layers of coquinas and lake mudstones.

The Morro do Chaves Formation is composed of bivalve coquinas of *Anodontophora* sp., *Gonodon* sp., *Psammobia* sp., *Nucula* sp. and *Astarte* sp. (Borges 1937; Oliveira 1937), and small gastropods. The bivalves developed in shallow and oxygenated waters. After their death, due to strong storms, the shells were reworked and accumulated like bars, washed over fans and beaches, and transported to the coastline (Mizuno et al. 2018; Muniz and Bosence 2018; Oliveira et al. 2019). According to Rigueti et al. (2020), the facies of the Morro do Chaves Formation indicate low gradient deposition and a high energy coastline. This is supported by the predominance of coastal sediments influenced by storms (Favoreto et al. 2021).

Several previous studies focused on the taphonomy of coquinas. For example, Pettijohn (1957) described coquinas as carbonate rocks consisting of fossil fragments (totally or partially) that were transported and then subjected to mechanical stress. However, Schäfer (1972) characterized coquinas as a concentration of shells and/or fragments exclusively, deposited by the action of a transport agent. Both studies suggested that the composition, stratum geometry and distribution of coquinas is governed by the laws of transport and sedimentation, instead of biological laws. The views of Schäfer (1972) are supported by Tavares et al. (2015), who noted that data from the same formation indicated that the coquinas were only formed by shells (pristine and fragmented). This view is reinforced by the presence of siliciclastic material in coquina beds, reaching values of about 50% of the siliciclastic matrix (Tavares et al. 2015; Corbett et al. 2016).

3 Material and Methods

3.1 Coquinas from the Morro do Chaves Formation

For our study, we used four coquina core plugs taken from a continuous core (UFRJ 2-SMC-02-AL), drilled at Atol Quarry, located in the city of São Miguel dos Campos in the Brazilian state of Alagoas. The samples were taken at depths having more terrigenous material, while especially considering plugs with similar porosities but significantly different permeability values. The samples, provided by the Laboratory of Sedimentary Geology (LAGESED) of UFRJ, were 2.5 cm in diameter and up to 4.5 cm in height (Fig. 1). Since the MICP and XRD experiments are destructive techniques, subsamples were taken from areas adjacent to the drilled parts of the cores, as can be seen in Fig. 2.

3.2 Thin Sections

Microscopic characterizations of the selected samples were performed using thin sections with standard size slices (4.5 × 2.5 cm), made from cross-sections of the core plug samples. They were impregnated with blue epoxy resin to fill the pores of the rocks, thereby highlighting and facilitating the interpretation of the types of pores. A Zeiss



Fig. 1 Samples used in this study showing different apparent textures and pore structures at their surfaces

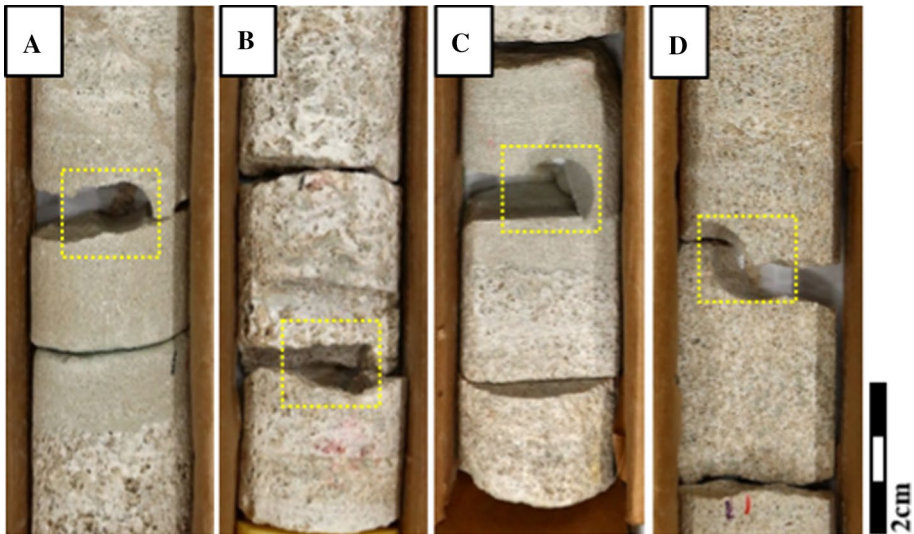


Fig. 2 Macroscopic photographs of the cores from UFRJ 2-SMC-02-AL where the samples and subsamples (yellow dashed line) were drilled: **a** sample 80; **b** sample 80.95; **c** sample 94.4; **d** sample 98.55

optical microscope, model Axio Imager 2 under polarized light, was used for the analysis. The coquinas were classified lithologically according to the scheme by Grabau (1904), which divides sediments into calcirudites with a particle size greater than 2 mm, calcarenites with granulometry between 2 and 0.0625 mm, and calcilitites with granulometry less than 0.0625 mm (Table 1). We further classified pores using the scheme of Choquette and Pray (1970) who employed geological concepts concerning the carbonate pore space, while also emphasizing the importance of pore genesis. The pores were evaluated using a digital image analysis approach. Following Pal et al. (2022), the pores were binarized and analyzed using Fiji-ImageJ, a free and open-source program (Kuva et al. 2012), to determine average pore sizes. (Fig. 3). The images were acquired using a Zeiss optical microscope, model M2m, under parallel polarized light and with a lens having a magnification of 5x. The pore types and grain textural classes are listed in Table 1 using the pore type nomenclature of Choquette and Pray (1970) and the grain size classification of Wentworth (1922).

Table 1 Classification of the four thin sections according to Grabau (1904), pore types according to Choquette and Pray (1970) and grain sizes according to Wentworth (1922)

Sample	Classification	Description	Pore type	Grain size	Diagnosis
80	Calcarenite	<i>Rock composition:</i> 68% terrigenous, 20% bivalves, 12% calcite cement <i>Composition:</i> 48% monocristalline quartz, 8% mud siltite peloid, 7% polycristalline quartz, 2% metamorphic lithoclasts, 2% siltite intraclasts, 1% feldspar (microcline and plagioclase) and TR mica (muscovite) <i>Terrigenous constituents:</i> fine to very coarse sand, medium average, subangular to rounded, moderately sorted <i>Carbonatic constituents:</i> The bivalves are mostly fragmented ($\pm 80\%$), with shells in a concordant orientation (regarding the bedding plan) and very coarse-grained sand	Moldic Vuggy Interparticle	Medium sand	Non-fabric selective dissolution, significantly increasing the size of the pores, and generating vuggy porosity. Poikilotopic calcite cement partly obliterated interparticle porosity
80.95	Calcirudite	<i>Rock composition:</i> 82% bivalves, 10% sparry calcite cement, 8% terrigenous <i>Carbonatic constituents:</i> whole bivalve shells well preserved. Rarely disarticulated and fragmented bivalves. Chaotic orientation of bivalve shells and fragments, with slight subparallel arrangement of bivalve shells	Vuggy Moldic	Coarse sand	Chemical compaction resulted in some sutured contacts between bivalves decreasing the porosity locally. Two intense dissolution stages were observed: (1) fabric selective, generating moldic porosity in bivalve bioclasts, and (2) non-fabric selective, which generated vuggy porosity
94.4	Sandstone	<i>Rock composition:</i> 70% terrigenous, 20% bivalves and 10% cement <i>Composition:</i> 39% monocristalline quartz, 5% mud siltite peloid, 14% polycristalline quartz, 5% metamorphic lithoclasts, 2% siltite intraclasts, 5% microcline and 2% mica (muscovite and biotite) <i>Constituents:</i> very fine to fine sand, high sphericity, well sorted. The bivalves are 100% fragmented, an agreeable orientation. Granulometry size coarse sand to granule. Well selected	Interparticle	Fine sand	Non-fabric selective dissolution, significantly increasing the pore system generating vuggy porosity. Late cements like calcite in blocky mosaic and poikilotopic obliterated the interparticle porosity, decreasing the connectivity between the pores

Table 1 (continued)

Sample	Classification	Description	Pore type	Grain size	Diagnosis
98.55	Calcarenite	<p>Rock composition: 85% bivalves, gastropod (Trace), 15% sparry calcite cement</p> <p>No terrigenous constituents</p> <p>Carbonatic constituents: whole and rare fragmented disarticulated bivalves. Parallel alignment (incipient physical compaction) was observed</p>	Vuggy	Coarse sand	Two intense dissolution events were observed: (1) fabric selective, generating moldic porosity in bivalve bioclasts, with an early (eogenetic) character, and (2) non-fabric selective character generating secondary vuggy porosities. The second dissolution event was more intense and promoted connections between moldic and vug pores, thereby increasing the permeability. Cements of late character, such as poikilotopic calcite, obliterated the vug pores (event after dissolution), but did not show much expressiveness

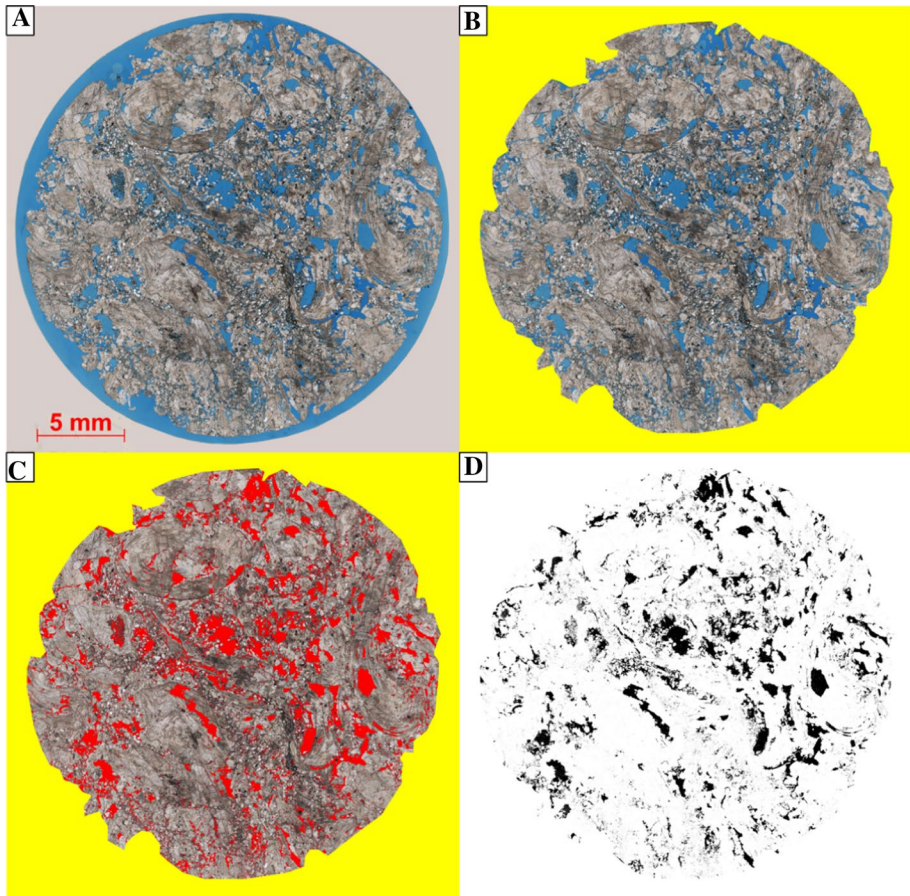


Fig. 3 Image processing workflow used for the pore size calculations: **a** scan of sample 80.95 thin section; **b** digital image of sample 80.95 with the area of interest cut from the ImageJ program; **c** digital image of sample 80.95 after setting the threshold and selecting all pores of the thin section; **d** digital image of sample 80.95 binarized, with the black pixels representing the pores

3.3 X-Ray Diffraction (XRD)

The mineralogy of the selected plug samples was determined using a Bruker-D4 Endeavor diffractometer using the following conditions: CoK α sealed tube ($\lambda=0.179021$ nm), generator operated at 40 kV and 40 mA, goniometer speed of 0.01° 2θ step with a counting time of 0.5 s per step, and collected from 4° to 90° 2θ with a LynxEye position-sensitive detector. Results were interpreted by comparisons with the standard spectra contained in the ICDD Database (2019) of the Bruker Diffrac EVA 5.0 software. The mineral phases were subsequently quantified in terms of fundamental parameters (Cheary and Coelho 1992) by using software DIFFRAC.TOPAS version 5.0 from Bruker-AXS based on the Rietveld refinement method. The preparation and experiments were carried out at the Centro de Tecnologia Mineral (CETEM).

3.4 Routine Core Analysis (RCAL)

The samples were initially subjected to thorough cleaning and extraction of fluids previously present in the pore system, an essential step for complete removal of impurities in the samples. For this stage, we employed the Soxhlet method using pure toluene for removing hydrocarbons, and pure methanol for the extraction of salts. The entire process lasted about 3 months, and the inspections were performed by UV light for oil fluorescence and 10% AgNO₃ solution for salt detection (McPhee et al. 2015). An advantage of this technique is the complete removal of natural contaminants in a continuous and unsupervised manner, without causing damage to the samples (Mcphee et al. 2015). After cleaning, the samples were dried in an oven at a controlled temperature of 60 °C for 24 h.

3.5 Nuclear Magnetic Resonance (NMR)

The NMR experiments were carried out in a low-field spectrometer GeoSpec2 (Oxford Instruments, UK), having a magnetic field equal to 0.047 T and a frequency of 2 MHz. All acquisition controls were implemented using GIT software (Green Imaging Technologies, Fredericton, Canada). For this analysis, the samples were saturated with a 30,000 ppm solution of KCl. The analyses were carried out using transversal relaxation measures (T_2) obtained by using CPMG pulse sequences, which are commonly used in petrophysical studies (e.g., Fleury and Romero-Sarmiento 2016; Lima et al. 2020). A CPMG pulse sequence consists of a 90° radio frequency pulse followed by a pulse train of 180°, delayed by $\pi/2$ of the first pulse. Echo intensity measurements were performed with a signal/noise ratio above 100.

3.6 Mercury Injection Capillary Pressure (MICP)

The MICP experiments were performed using an Autopore IV 9500 (Micromeritics Instruments Co.). Since MICP is a destructive technique, the subsamples for these tests were taken from areas adjacent to the plugs used for the other laboratory experiments. The fragments were subjected to a vacuum of 50–900 μm inside a penetrometer filled with mercury. The pressure was increased up to a final value of 60,000 psi in order to obtain accessible pore volumes at different pressures. The non-wetting mercury will first invade the larger pores but with increasing pressures slowly moves into the entire pore system.

3.7 X-Ray Microtomography (microCT)

MicroCT scanners provide non-destructive 3D images for investigating the internal structure of materials, thereby allowing investigations of the pore structure at scales ranging from micrometers up to a few millimeters. Image acquisitions were performed using CoreTOM equipment (Tescan/XRE) with a 14 μm voxel size, while the images were reconstructed using the Aquila reconstruction software (Tescan/XRE). Image processing was carried out using Avizo 9.5 (Thermo Fisher Scientific), by which the pores are identified and separated from the sample's mineral framework using threshold tools (Otsuki et al. 2006) as shown in Fig. 4. Segmentation of the image was performed according to the match of the NMR and MICP curves, as reported at Lima et al. (2020). After this, the

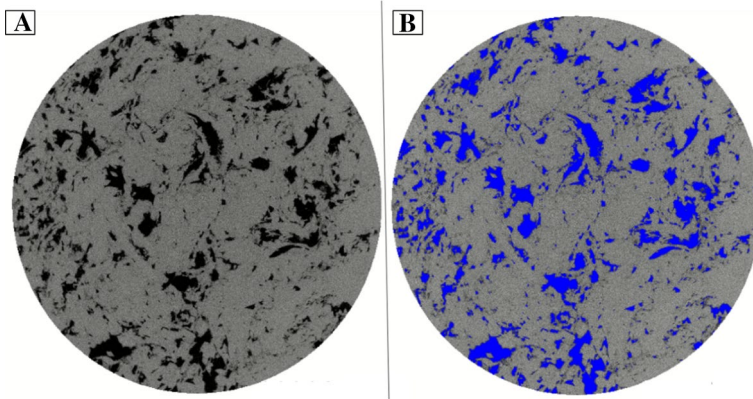


Fig. 4 MicroCT slices of sample 98.55 with a voxel size of 14 μm : **a** Gray scale image with pores in black and the rock matrix in gray; **b** Grayscale image with the segmented pores in blue

pore structure and topology were analyzed by transforming the pore space into a skeleton showing individual pores and throats in the pore network (Pudney 1998; Wildenschild and Sheppard 2013). The skeleton was used subsequently for modeling the pore network using the PoreStudio software, an update of the PoreFlow model of Raouf et al. (2013). PoreStudio results include not only the absolute permeability, but other data such as the digital porosity of the samples, the flow length in the coquina pore network, the pressure distribution, and the Darcy velocity. The software provides numerical output as well as 2D or 3D graphical representations, which can be visualized using Paraview (Ayachit 2015).

4 Results and Discussion

Descriptions of the thin sections are shown in Table 1. Between 20 and 85% of all samples were found to consist of whole or fragmented bivalves. The terrigenous material in samples 80 and 94.4 was estimated to be approximately 70%. The pore classification indicated moldic and vug porosities in most samples, with only sample 94.4 showing a predominant interparticle porosity. Details of the thin sections are shown in Fig. 5.

The XRD results indicated that the samples were composed mainly of calcite, with some presence also of quartz, feldspar and clays (Fig. 6). Samples 80 and 94.4 had a high percentage of quartz and other terrigenous minerals, which may have produced some changes in their petrophysical characteristics. Quartz contents ranged from 1 to 37%, feldspars from 0.1 to 5%, and clays from 1 to 7.6%.

Results of the routine core and NMR analyses, as well as those obtained using pore-scale network modeling, are shown in Table 2. The routine core analysis provided measures of porosity and permeability, which were used for calibrating the other petrophysical data (Lima et al. 2020). Table 2 shows that the samples used in this study had very similar porosities (ranging between 16 and 19%), but wide variations in their permeability values (between 24 mD all the way up to 650 mD). The wide range in permeability with small variations in porosity is characteristic of coquinas from the Morro do Chaves Formation, as reported earlier also by Corbett et al. (2016). This demonstrates the importance of

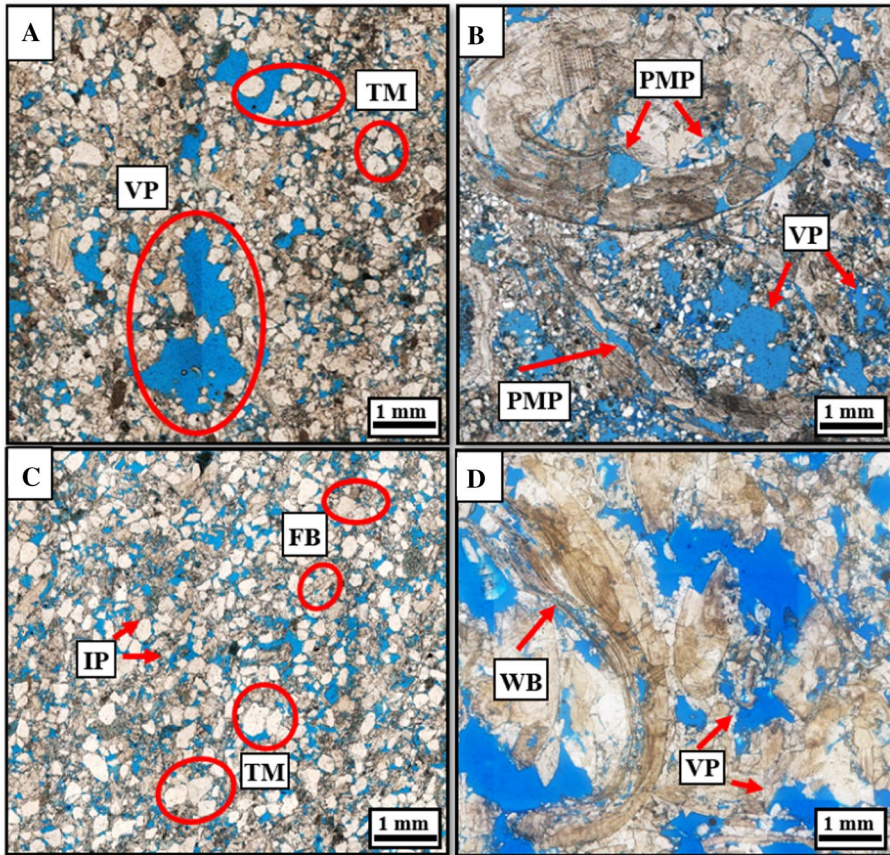


Fig. 5 Photomicrographs of the thin sections in plane-polarized light: **a** Sample 80 (calcarenite) with highlighted vug pores (VP) and terrigenous material (TM); **b** Sample 80.95 (calcirudite) with identified vug pores (VP) and partial moldic porosity (PMP); **c** Sample 94.4 (sandstone) with highlighted interparticle pores (IP), fragmented bivalves (FB) and terrigenous material (TM); and **d** Sample 98.55 (calcarenite) with identified whole bivalves (WB) and vug pores (VP)

accurate and detailed studies of these rocks to obtain a more complete understanding of their structure.

Porosities obtained using NMR agreed well with those derived using the routine core analyses, with a difference of only about 2% (e.g., Souza 2012). PoreStudio pore network modeling produced porosities that were lower than the routine core measurements. This was expected since the microCT resolution did not allow visualization of the entire pore space of the samples but only for pore radii above 7 μm . Regarding the calculated permeabilities, samples 80.95 and 94.4 showed values that agreed closely with the routine results. Samples 80 and 98.55, on the other hand, showed lower values than the routine core data. These results can be explained by the imaging resolution in that some of the pores in the pore network responsible for flow within these two samples were below the imaging resolution (Godoy et al. 2019). Still, the results are quite satisfactory (Table 2).

An important outcome of the NMR measurements is the pore size distribution of the rock samples. Once a saturation above 95% is obtained, estimates of the pore

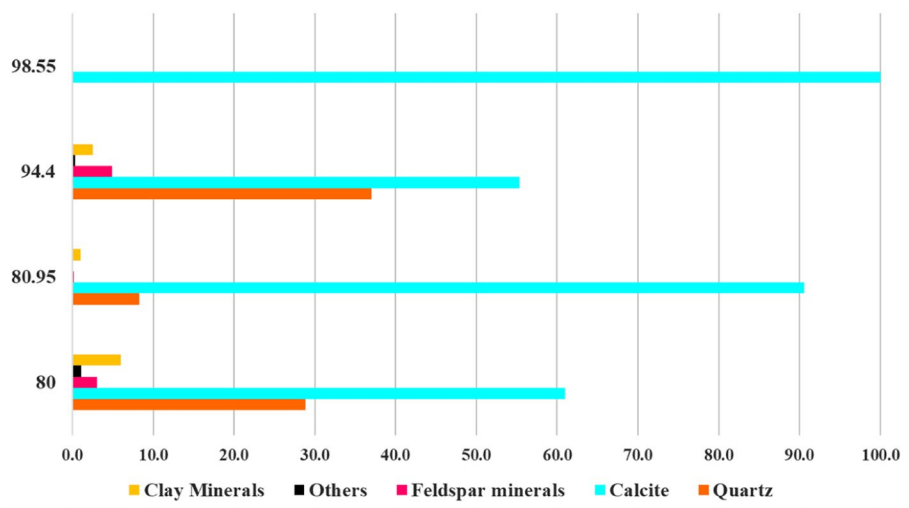


Fig. 6 Bar chart of XRD results showing a predominance of calcite in the different samples

Table 2 Porosity (ϕ) and permeability (k) results obtained using routine core analysis (RCAL), NMR and PoreStudio modeling

Sample	ϕ_{RCAL}	k_{RCAL}	ϕ_{NMR}	$\phi_{PoreStudio}$	$k_{PoreStudio}$
80	16%	24 mD	15.4%	6.0%	7.0 mD
80.95	19%	504 mD	17.5%	12.6%	462.5 mD
94.4	18.4%	103 mD	17.9%	11.6%	10.5 mD
98.55	18.4%	650 mD	18.0%	13.4%	498.6 mD

size distribution can be acquired using the NMR transverse relaxation time distribution curves (T_2). Figure 7a shows that results obtained for samples 80 and 94.4 were very similar as those of samples 80.95 and 98.55. Following pore size partitioning as defined by Silva et al. (2015), samples 80 and 94.4 had most of their pores in the hybrid meso-/macropores region (between 100 and 1000 ms), while the other samples concentrated more in the macroporosity region (above 1000 ms). An important aspect of the NMR experiments is the relaxation time of the saturating fluid. The KCl brine presented a relaxation of 2500 ms, contributing to the interpretation of the macropores, which relaxed after 1000 ms. These values covered part of the pores of samples 80.95 and 98.55, thus making the T_2 values less reliable as indicated by Lima et al. (2020). The microCT images, on the other hand, provide a better definition of the largest pores and hence give greater confidence in the obtained pore sizes.

A useful analysis complementary to NMR is characterization of the distribution of pore apertures (e.g., their radii) using MICP. With this approach the entire pore system represented by pore bodies (corresponding to the largest voids) and pore throats (connections between the pore bodies) can be evaluated (Yuan and Rezaee 2019). The distribution of pore throats from the MICP measurements (provided in Fig. 7b) shows that of the four samples, sample 94.4 had throats with the smallest radius. Despite having different pore sizes as reflected by the T_2 curves, samples 80 and 80.95 had similar pore

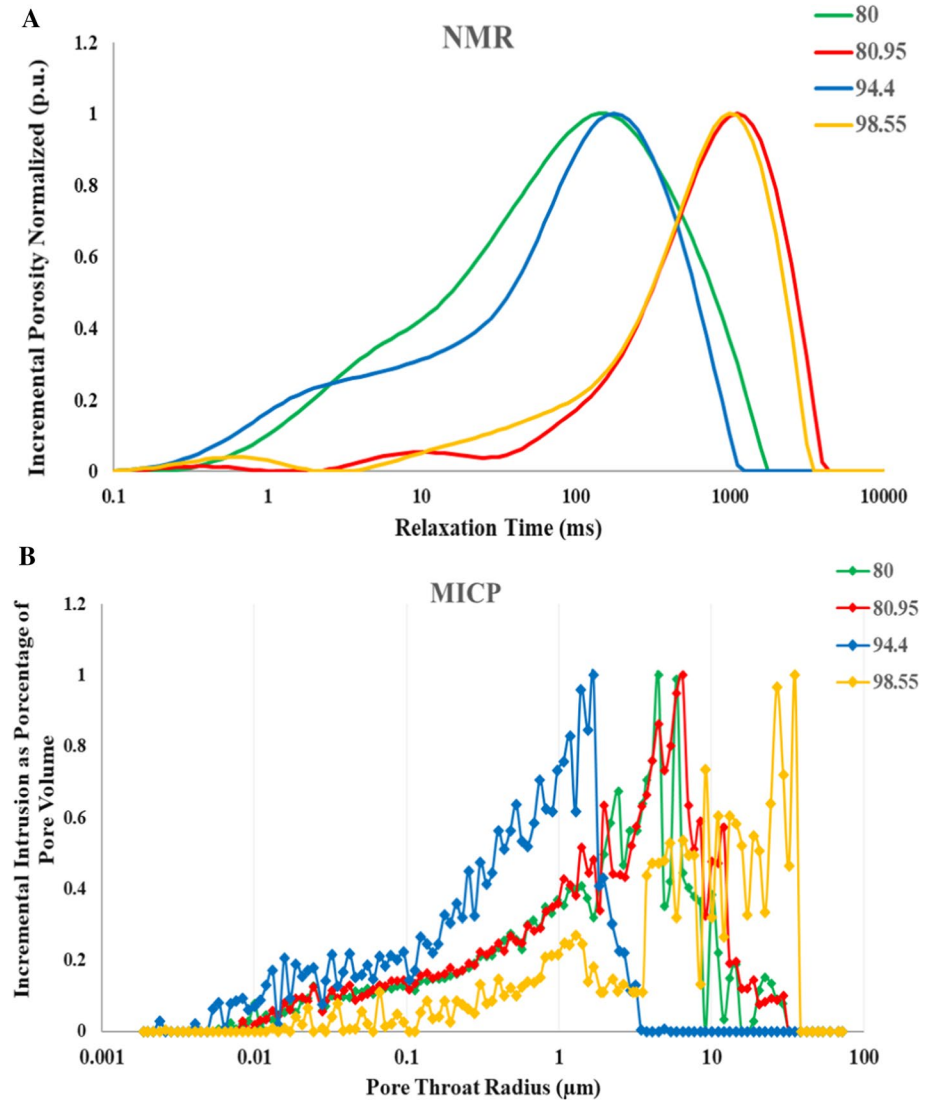


Fig. 7 a NMR graphs of the samples; b pore radii distributions of the MICP measurements

throat sizes. Sample 98.55, on the other hand, had the largest throat radii in the group, which explains its higher permeability (the highest of our samples).

To better compare the results, we constructed parallel coordinate plots for the various parameters obtained for each sample. The value of each parameter was for this purpose normalized by its highest value of the four samples. As can be seen in Fig. 8a, the samples had similar porosities but significantly different permeabilities. Samples 80 and 94.4, which had higher percentages of quartz, did not only have much lower permeability values, but also relatively low values of the average pore throat (APT) and the average pore size (APS). This information, together with observations from the thin sections and the plots in

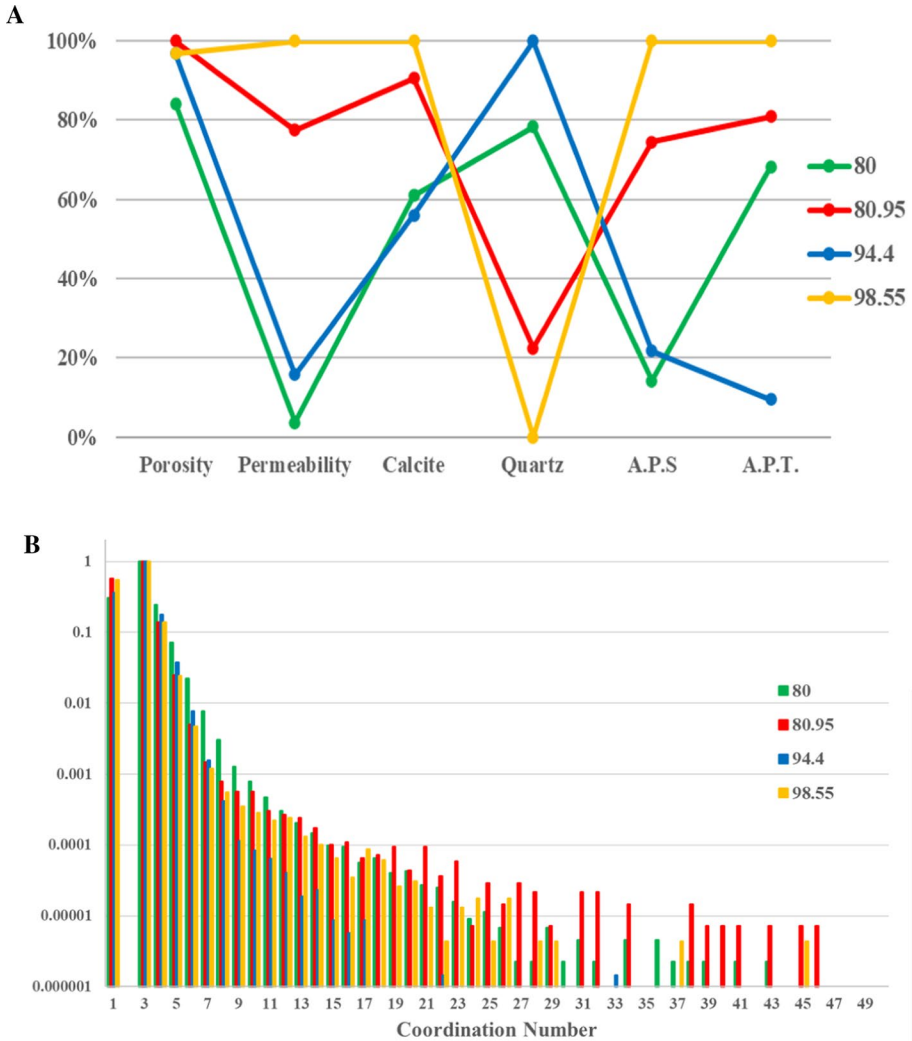


Fig. 8 **a** Parallel coordinate plot showing results of the porosity and permeability from the routine core analyses, the XRD results (calcite and quartz contents), average pore sizes (APS) based on the NMR experiments, and average pore throats (APT) based on the MICP measurements. The data were normalized by the highest value of each parameter; **b** Histogram of the coordination number of the four samples based on the pore network modeling results

Fig. 7, shows that terrigenous material and the high shell fragmentations in these samples contributed to the permeability reductions, as compared to the other samples. On the other hand, samples 80.95 and 98.55 were composed of whole bivalves, while containing a low percentage of terrigenous minerals. Bioclastics subjected to diagenetic processes presumably caused secondary porosity, mainly vug and moldic pores (within the range of coarse sand) which increased the pore space and ultimately the permeability of these samples.

Another aspect shown in the parallel coordinate plots is the average pore throat radius. As seen by the RCAL results (Table 1), samples 80 and 80.95 had different permeabilities

(24 mD and 504 mD, respectively). However, the MICP curves and parallel coordinate plots seem to contradict this finding in that the samples had very similar pore throat radii, which is the main component responsible for flow within the rocks. To investigate this inconsistency, other factors that impact fluid flow within the pore network were investigated, such as the connectivity among different pores as represented by the coordination number distribution (Fig. 8b). This number, also called the pore connectivity, represents the average number of pore bodies that are connected to adjacent pores (Sahimi et al. 2012). They are a fundamental characteristic of pore networks and have a real impact on hydraulic conductance calculations of porous rocks (Chen et al. 2003; Vasilyev et al. 2012). The connectivity information of the samples was extracted from the skeletons of the samples (Godoy et al. 2019). Sample 80 was found to have a relatively large number of pores belonging to pore systems with low coordination numbers. Sample 80.95, on the other hand, had more pore volumes associated with high coordination numbers, thus benefiting its permeability.

Table 2 shows that the modeling results were consistent with the routine core analyses, considering the microCT resolution that was used (14 μm voxel size). This provided confidence for us to use the data extracted from the skeletonization to better understand why the connectivity of the various pore systems produced different permeabilities of the samples. Using ParaView (Ayachit 2015), the pore networks of the samples could be visualized and further analyzed to identify the pore bodies that most connected to the overall pore system. This made it possible to select and quantify the connected pore clusters, in addition to enabling visualization of the main pore cluster that connected with the bottom and the top of a sample (i.e., from the inlet all the way to the outlet face of a sample), and hence was responsible for most of the established flow within the pore system.

Figure 9 presents the 3D pore structures of the four samples, showing the permeability pathways along clusters of connected pores. Figure 9a illustrates the pores of sample 80. We noticed that more pores at the top of the sample had smaller diameters (shown by blue tubes). The bottom, however, showed a gradual increase in the pore diameters, which likely was due to pores created by non-fabric selective dissolution, which were important in terms of increasing the pore space by generating vuggy porosity (shown by yellow spheres). Remarkably, the middle of the sample showed a strip of gray-colored pores disconnected from the main conducting pore cluster. We conclude that this zone in the middle of the sample is responsible for the flow reduction, thereby causing a substantial overall permeability reduction of this sample. The cementation could be seen at its thin section (Fig. 10). As reported in Table 1, one of the diagenetic processes identified for sample 80 was poikilotopic calcite cementation. Even though sample 80 had a wide range of pore throats (Fig. 7b), cementation negatively affected the pore system by partially closing interparticle pores and reducing the connectivity of the system. The abundance of terrigenous material in the cemented region, consisting of fine to very coarse sand, subangular to rounded grains and moderately sorted, resulted in different flow properties as compared to the other samples, thus reducing the permeability of this sample.

Figure 9b shows the main clusters of pores identified in sample 80.95. The 3D structure shows a much better pore interconnection, consistent with the higher permeability of this sample. As noted earlier, sample 80.95 contained moldic and vug pores (within the range of coarse sand), represented by yellow and orange spheres in the plot. The gray clusters of disconnected pores did not compromise the overall connections by being present only in relatively isolated parts of the sample.

Figure 9c shows the pore structure of sample 94.4. This sample had a far more homogeneous distribution of pores, but contained also a few large disconnected clusters (in gray)

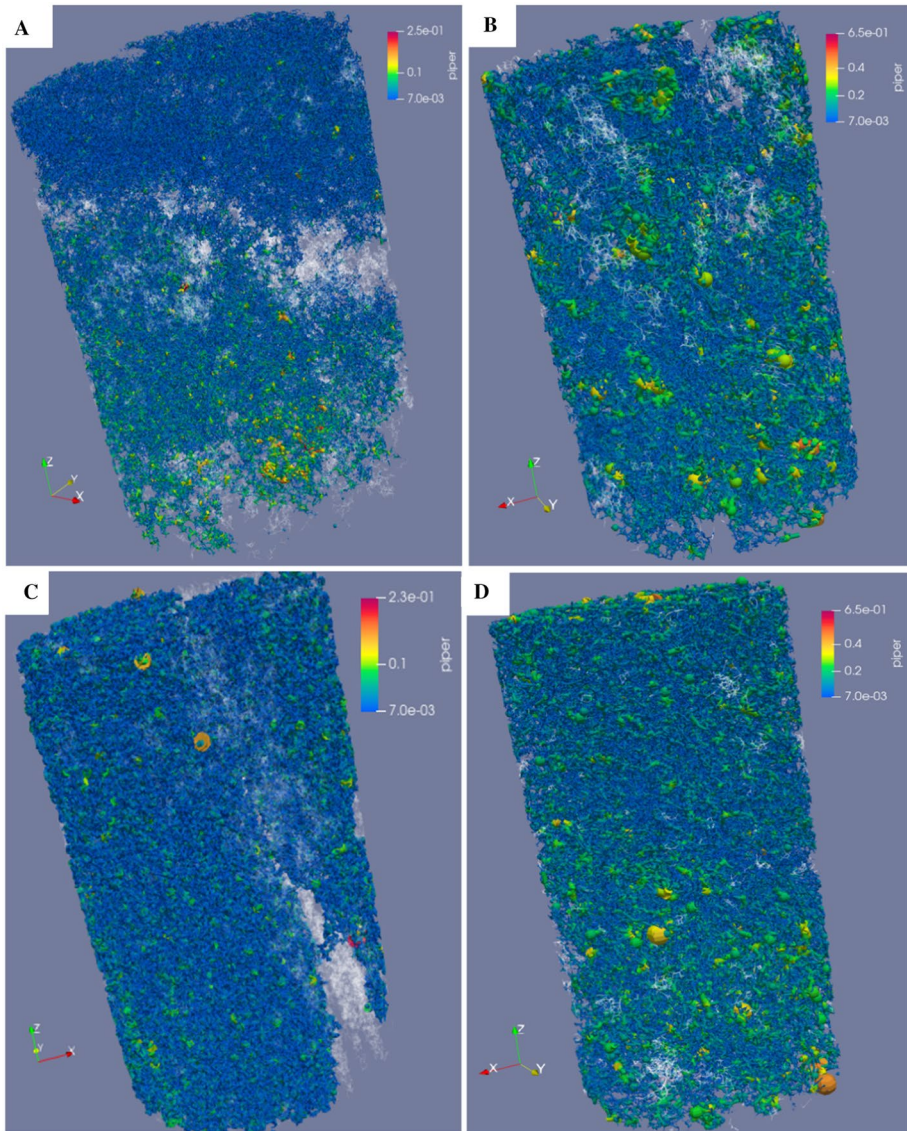


Fig. 9 Pore structure and distribution of the main (conducting) pore clusters of the four samples, with non-conducting (disconnected) pores shown in gray: **a** Sample 80 with a large fraction of disconnected pores; the largest conducting pores of this sample are shown in yellow, **b** Sample 80.95 showing also some disconnected pores (in gray); the largest pores are shown in orange, **c** Sample 94.4 showing a more homogeneous distribution of the pores, but also a zone with disconnected pores (in gray); the largest pores in the sample are shown in green, and **d** Sample 98.55 showing more disconnected pores (in gray), with the largest pores displayed in orange. The scale bar indicates pore throat radii in millimeters

within and aside from the main cluster (in blue), which caused the permeability of the digital sample to become only 10% of the routine (RCAL) value (Table 2). The terrigenous material of this sample consisted of very fine to fine well-sorted sand grains. The

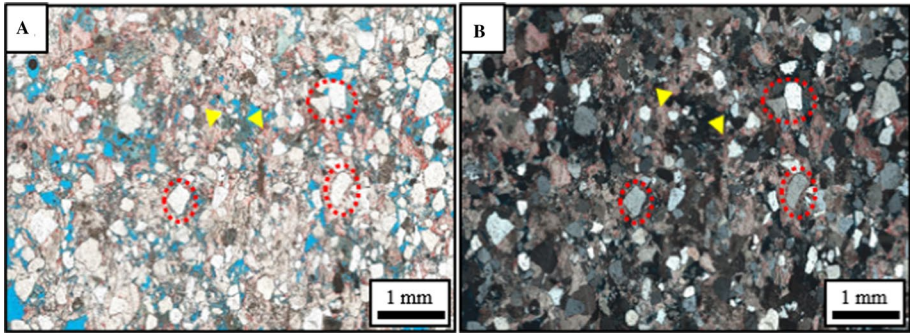


Fig. 10 Photomicrographs of sample 80 showing poikilotopic calcite cement (yellow arrows) and quartz grains (red dashed circles): **a** under plane-polarized light; **b** under cross-polarized light

interparticle porosity of the terrigenous material was well connected and the pore sizes more similar (on average around $16\ \mu\text{m}$), which explains the higher measured permeability of this sample as compared to sample 80 (which also contained elevated amounts of terrigenous content). The vuggy porosity (green spheres in Fig. 9c), thought to result from selective dissolution, had little effects on flow since the larger pores were not connected.

Figure 9d shows the pore groups of sample 98.55, which recorded the highest permeability of the four samples. The higher permeability is consistent with the connected relatively large pores of this sample (yellow and orange spheres), and with only a few clusters of isolated pores present (in gray). The thin section of this sample earlier indicated that the large pores may have been formed by extensive fabric selective and non-fabric selective dissolution processes, leading to moldic and vuggy porosity, respectively, with pore sizes of about $0.6\ \text{mm}$. As noted in Table 1, a second (diagenetic) stage must have promoted a better interconnectivity between the pores, classified as vugs (in green), which favored a higher permeability.

Since its pore characteristics were different from the others, we analyzed statistically the skeleton information of sample 80 more closely. Results are shown in Fig. 11. The strip of disconnected pores occurred in a region of the sample having the largest amounts of cementation, which caused a reduction in flow and consequently in a lower permeability. Figure 11a shows the pore network of sample 80. The pore space was divided into 20 sub-volumes as highlighted in the figure. Sub-volume 13 (shown using a pink color) was located above the cemented region, and sub-volume 5 (in green) below this region. In the pink section, one can identify a reduction in the porosity of the central region of the slice, probably a result of more terrigenous material. By contrast, the green section showed a much better distribution of pores.

Figure 11b–d shows the profiles of relevant flow properties of sample 80. The yellow arrows point to characteristics of sub-volume 13. For example, a reduction occurred there in the percentages of pore bodies and pore throats associated with a lower count of these pores, and relatively low average sizes of the pore body and pore throat radii. These data are directly linked to the presence of terrigenous material, which reduced the pore diameters and caused obstructions to flow due to the shapes and granulometries of the grains. The purple arrows near sub-volume 5 show the change in the pore characteristics below the cemented region. Compared to sections just above this Sect. 5, an increase occurred in the pore body and pore throat percentages, along with a slight reduction in their population

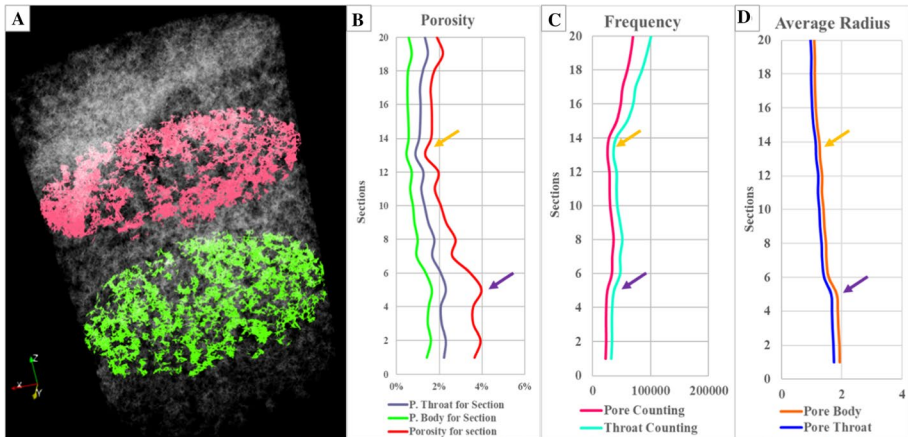


Fig. 11 **a** Pore space of sample 80. The sample was divided into 20 sub-volumes for analysis. The pink slice corresponds to sub-volume 13 and the green slice to sub-volume 5; **b** plot showing by section the pore body porosity (green line), the pore throat porosity (gray line) and the total porosity (red line); **c** plot showing by sub-volume the population of pore bodies (pink line) and pore throats (cyan line); **d** plot showing the average pore body and pore throat radii. The arrows in plots (**b**), (**c**) and (**d**) identify the sub-volumes highlighted in the image

and an increase in the average pore body and pore throat radii. Since the radii have more influence on the porosity (cubic effects), they end up being more relevant as compared to the frequency, which only has linear effect on the porosity.

5 Conclusions

Our research aimed to identify the petrophysical differences in carbonate rock samples having different percentages of terrigenous material. For our study, we used four samples of coquinas obtained from a continuous core from the Morro do Chaves Formation. Thin sections and XRD analysis were used for a more accurate interpretation of the geological characteristics of the samples, and for petrophysical characterizations were used routine core analysis, NMR, MICP and microCT images. The samples were found to have large variations in permeability, even though they had similar porosities, a fact directly linked to the percentages of terrigenous material in the samples. Rocks with more terrigenous material, mainly quartz, showed lower permeabilities, directly linked to the fragmentation, granulometry and sorting of this mineral. Samples with little terrigenous material (quartz) on the other hand exhibited higher permeabilities due to low fragmentation of bioclasts and diagenetic processes. Carbonate minerals (in our case calcite) seem to be susceptible to dissolution as reflected by an increase of pore body and pore throat size (moldic and vuggy pores).

The NMR results showed that samples 80 and 94.4 (the more quartz-rich samples) had most of their pores in the meso-/macropore range, while samples 80.95 and 98.55 with their lower quartz percentages had most pores in the macropore range. The pore distributions were found to be consistent with the measured permeability values since samples 80 and 94.4 had lower values compared to the others. MICP information, on the other hand, showed that the pore throats of sample 94.4 had smaller diameters, samples 80 and 80.95 had similar diameters, and sample 98.55 had the largest diameters of the set.

To understand why samples with similar throats had different permeabilities, microCT images were used to generate skeletons identifying both the 3D pore spaces and their connections. From the pore coordination number, a frequency histogram could be created, which showed that sample 80 exhibited a large fraction of pore bodies with a lower coordination number, while sample 80.95 showed more pore bodies with a higher coordination number, thus explaining the permeability differences.

Since sample 80 presented a different pore system than the others as shown by the skeletons generated from the microCT images, information about porosity percentages, pore body and pore throat populations, and average pore body and pore throats radii were analyzed. For our study, the skeleton was divided into 20 sub-volumes. Two sub-volumes were highlighted: sub-volume 13, above the cemented region, and sub-volume 5, below this region. Cementation was found to directly impact the petrophysical characteristics of the sample. Sub-volume 13 showed a lower pore percentage, and lower pore body and pore throat counts and radii. Sub-volume 5, on the other hand, showed an increase in the pore percentage and a reduction in the count of individuals, but an increase in the average radius. These characteristics are consistent with more terrigenous material, as well as the shape, granulometry, and sorting of these grains.

We conclude that the most complete geological information involving thin section and XRD information integrated with routine core analyses, NMR, MICP and pore network modeling using 3D images, provided optimal insight into the flow properties of the samples. Results show that diagenetic alterations and, more specifically, calcite dissolution and connected vuggy and moldic porosity formation, contributed to an increase in permeability as compared to samples with a higher percentage of terrigenous minerals. Those minerals are not only more resistant to diagenesis, but their shape, granulometry and sorting also impacts permeability.

Acknowledgements This research was carried out in association with ongoing R&D projects registered as ANP 19027-2, “Desenvolvimento de infraestrutura para pesquisa e desenvolvimento em recuperação avançada de óleo – EOR no Brasil” (UFRJ/Shell Brasil/ ANP) setting-up a advanced EOR Lab facility for R&D in Brasil, and ANP 20163-2, “Análise experimental da recuperação de petróleo para as rochas carbonáticas do pré-sal brasileiro através da injeção alternada de CO₂ e água”, with samples provided by Project SACL (Análise geológica sedimentar de sucessões carbonáticas do Cretáceo em uma bacia sedimentar brasileira (ANP n.18993-6), all sponsored by Shell Brasil under the ANP R&D levy as “Compromisso de Investimentos com Pesquisa e Desenvolvimento”. This study was financed in part by the Coordenação de Aperfeiçoamento de Pessoal de Nível Superior- Brasil (CAPES)—Finance Code 001, and carried out with the support of CNPq (National Council of Scientific and Technological Development, Brazil). We acknowledge Prof. Rodrigo Bagueira (UFF-LAR) for helping with saturating the samples and use of the NMR equipment. We further acknowledge CETEM (Centro de Tecnologia Mineral) for the XRD analysis. We also thank the research teams of LRAP/COPPE/UF RJ and LAGESED/UF RJ.

Funding This work was supported by Shell Brasil in association with ongoing R&D projects registered as ANP 19027-2 (UFRJ/Shell Brasil/ ANP) setting-up an advanced EOR Lab facility for R&D in Brasil, and ANP 20163-2.

Declarations

Competing interests The authors have no competing interests to declare that are relevant to the content of this article.

Open Access This article is licensed under a Creative Commons Attribution 4.0 International License, which permits use, sharing, adaptation, distribution and reproduction in any medium or format, as long as you give appropriate credit to the original author(s) and the source, provide a link to the Creative Commons licence, and indicate if changes were made. The images or other third party material in this article

are included in the article's Creative Commons licence, unless indicated otherwise in a credit line to the material. If material is not included in the article's Creative Commons licence and your intended use is not permitted by statutory regulation or exceeds the permitted use, you will need to obtain permission directly from the copyright holder. To view a copy of this licence, visit <http://creativecommons.org/licenses/by/4.0/>.

References

- Ahr, W.M.: *Geology of Carbonate Reservoirs: The Identification, Description, and Characterization of Hydrocarbon Reservoirs in Carbonate Rocks*, p. 296. Wiley, Hoboken (2008)
- ANP: Agência Nacional do Petróleo, Gás Natural e Biocombustíveis. Anuário estatístico brasileiro do petróleo, gás natural e biocombustíveis (2018). <http://www.anp.gov.br/publicacoes/anuario-estatistico/anuario-estatistico-2018>.
- Ayachit, U.: *The Paraview Guide: A Parallel Visualization Application*. Kitware Inc, New York (2015)
- Azambuja, N.C., Arienti, L.M.: Guidebook to the rift-drift Sergipe-Alagoas, passive margin basin, Brazil. In: *The 1998 American Association of Petroleum Geologists International Conference and Exhibition* (1998).
- Basan, P.B., Lowden, B.D., Whattler, P.R., Attard, J.J.: Pore-size data in petrophysics: a perspective on the measurement of pore geometry. *Dev. Petrophys. Geol. Soc. Lond. Spec. Publ.* **122**, 47–67 (1997). <https://doi.org/10.1144/gsl.sp.1997.122.01.05>
- Borges, J.: Pesquisas de fósseis em Jabotão e Morro do Chaves, Brasil: Serviço Geológico e Mineralógico. *Notas Preliminares e Estudos* **15**, 7–11 (1937)
- Cainelli, C., Mohriak, W.U.: Some remarks on the evolution of sedimentary basins along the Eastern Brazilian Continental Margin. *Episodes* **22**(3), 206–216 (1999)
- Campos Neto, O.P.A.C., Lima, W.S., Cruz, F.E.G.: Bacia de Sergipe-Alagoas. *Boletim De Geociências Da Petrobras* **15**, 405–415 (2007)
- Carvalho, M.D., Praça, U.M., Telles, A.C.S.: Bioclastic carbonate lacustrine facies molds in the Campos Basin (lower Cretaceous), Brazil. In: Gierlowski-Kordesch, E.H., Kelts, K.R. (eds.) *Lake Basins Through Space and Time*. AAPG Studies in Geology, 46 (2000)
- Ceraldi, T.S., Green, D., 2016. Evolution of the South Atlantic lacustrine deposits in response to Early Cretaceous rifting, subsidence and lake hydrology. In: T.S. Ceraldi, R.A. Hodgkinson, and H. Backe G (eds), *Petroleum Geoscience of the West Africa Margin*, vol. 438. Geological Society, Special Publications, London. <https://doi.org/10.1144/SP438.10>
- Chandra, V., Barnett, A., Corbett, P., Geiger, S., Wright, P., Steele, R., Milroy, P.: Effective integration of reservoir rock-typing and simulation using near-wellbore upscaling. *Mar. Pet. Geol.* **67**, 307–326 (2015). <https://doi.org/10.1016/j.marpetgeo.2015.05.005>
- Cheary, R.W., Coelho, A.: A fundamental parameters approach to x-ray line-profile fitting. *J. Appl. Cryst.* **25**, 109–121 (1992). <https://doi.org/10.1107/S0021889891010804>
- Chen, S.C., Lee, E.K., Chang, Y.I.: Effect of the coordination number of the pore-network on the transport and deposition of particles in porous media. *Sep Purif Technol* (2003). [https://doi.org/10.1016/S1383-5866\(02\)00096-5](https://doi.org/10.1016/S1383-5866(02)00096-5)
- Chinelatto, G.F., Belila, A.M.P., Basso, M., Souza, J.P.P., Vidal, A.C.: A taphofacies interpretation of shell concentrations and their relationship with petrophysics: a case study of Barremian-Aptian coquinas in the Itapema Formation, Santos Basin, Brazil. *Mar. Petrol. Geol.* (2020). <https://doi.org/10.1016/j.marpetgeo.2020.104317>
- Choquette, P.W., Pray, L.C.: Geologic nomenclature and classification of porosity in sedimentary carbonates. *AAPG* **54**(2), 207–250 (1970). <https://doi.org/10.1306/5D25C98B-16C1-11D7-8645000102C1865D>
- Corbett, P.W.M., Estrella, R., Rodriguez, A.M., Shoeir, A., Borghi, L., Tavares, A.C.: Integration of Cretaceous Morro do Chaves rock properties (NE Brazil) with the Holocene Hamelin Coquina architecture (Shark Bay, Western Australia) to model effective permeability. *Petrol. Geosc.* **22**(2), 105–122 (2016)
- Corbett, P.W.M., Wang, H., Câmara, R.N., Tavares, A.C., Borghi, L., Perosi, F., Bagueira, R.: Using the porosity exponent (m) and pore-scale resistivity modeling to understand pore fabric types in coquinas (Barremian-Aptian) of The Morro do Chaves Formation, NE Brazil. *Mar. Petrol. Geol.* **88**, 628–647 (2017)

- de Leite, C.O.N., de Assis Silva, C.M., de Ros, L.F.: Depositional and diagenetic processes in the pre-salt rift section of a Santos Basin area, SE Brazil. *J. Sediment. Res.* **90**(6), 584–608 (2020). <https://doi.org/10.2110/jsr.2020.27>
- Favoreto, J., Valle, B., Borghi, L., Dal'ób, P.F., Mendes, M., Arena, M., Santos, J., Santos, H., Ribeiro, C., Coelho, P.: Depositional controls on lacustrine coquinas from an early cretaceous rift lake: Morro do Chaves Formation, Northeast Brazil. *Mar. Petrol. Geol.* (2021). <https://doi.org/10.1016/j.marpetgeo.2020.104852>
- Fleury, M., Romero-Sarmiento, M.: Characterization of shales using T1–T2 NMR maps. *J. Petrol. Sci. Eng.* **137**, 55–62 (2016). <https://doi.org/10.1016/j.petrol.2015.11.006>
- Gao, H., Li, H.A.: Pore structure characterization, permeability evaluation and enhanced gas recovery techniques of tight gas sandstones. *J. Nat. Gas Sci. Eng.* (2016). <https://doi.org/10.1016/j.jngse.2015.12.018>
- Godoy, W., Pontedeiro, E.M., Hoerlle, F., Raouf, A., van Genuchten, M.T., Santiago, J., Couto, P.: Computational and experimental pore-scale studies of a carbonate rock sample. *J. Hydrol. Hydromech.* **67**, 372–383 (2019). <https://doi.org/10.2478/johh-2019-0009>
- Grabau, A.W.: On the classification of sedimentary rocks. *Am. Geol.* **33**, 228–247 (1904)
- Herlinger, R., Jr., Zambonato, E.E., de Ros, L.F.: Influence of diagenesis on the quality of lower cretaceous pre-salt lacustrine carbonate reservoir from Northern Campos Basin, offshore Brazil. *J. Sediment Res.* **87**, 1285–1313 (2017)
- Hoerlle, F.O.L., Rios, E.H., Silva, W.G.A.L., Pontedeiro, E.M., Lima, M.C.O., Corbett, P.W.M., Alves, J.L.D., Couto, P.: Nuclear magnetic resonance to characterize the pore system of coquinas from Morro do Chaves Formation, Sergipe-Alagoas Basin, Brazil. *Brazil. J. Geophys.* **36**(3), 1–8 (2018). <https://doi.org/10.22564/rbgf.v36i3.1960>
- ICDD, International Centre for Diffraction Data (2019). <https://www.icdd.com/>
- Jia, C.: Characteristics of Chinese petroleum geology: geological features and exploration cases of stratigraphic, foreland and deep formation traps. In: *Petroleum Geology of Carbonate Reservoir*, pp. 495–532. Springer, Berlin (2012). https://doi.org/10.1007/978-3-642-23872-7_12
- Kuva, J., Sitar-Kauppi, M., Lindberg, A., Aaltonen, I., Turpeinen, T., Myllys, M., Timonen, J.: Microstructure, porosity and mineralogy around fractures in Olkiluoto bedrock. *Eng. Geol.* **139**, 28–37 (2012). <https://doi.org/10.1016/j.enggeo.2012.04.008>
- Lima, B.E.M., de Ros, L.F.: Deposition, diagenetic and hydrothermal process in the Aptian Pre-Salt lacustrine carbonate reservoirs of the northern Campos Basin, offshore Brazil. *Sediment. Geol.* **383**, 55–81 (2019)
- Lima, M.C.O., Pontedeiro, E.M., Ramirez, M.G., Boyd, A., van Genuchten, M.T., Borghi, L., Couto, P., Raouf, A.: Petrophysical correlations for permeability of coquinas (carbonate rocks). *Transp. Porous Media* **135**, 287–308 (2020). <https://doi.org/10.1007/s11242-020-01474-1>
- Lønøy, A.: Making sense of carbonate pore systems. *Am. Assoc. Pet. Geol.* **90**(9), 1381–1405 (2006)
- Luna, J.L., Perosi, F.A., Ribeiro, M.G.S., Souza, A., Boyd, A., Almeida, L.F.B., Corbett, P.L.M.: Petrophysical rock typing of coquinas from the Morro do Chaves Formation, Sergipe-Alagoas basin (Northeast Brazil). *Braz. J. Geophys.* (2016). <https://doi.org/10.22564/rbgf.v34i4.883>
- Mephee, C., Reed, J., Zubizarreta, I.: Core sample preparation. In: *Core Analysis: A Best Practice Guide*, pp. 138–143. Elsevier, Amsterdam (2015)
- Mehmani, A., Verma, R., Prodanović, M.: Pore-scale modeling of carbonates. *Mar. Petrol. Geol.* (2020). <https://doi.org/10.1016/j.marpetgeo.2019.104141>
- Mizuno, T.A., Mizuasaki, A.M.P., Lykawka, R.: Facies and paleoenvironments of the Coqueiros Formation (Lower Cretaceous, Campos Basin): A high frequency, stratigraphic model to support the pre-salt “coquinas” reservoir development in the Brazilian continental margin. *J. South Am. Earth Sci.* **88**, 107–117 (2018). <https://doi.org/10.1016/j.jsames.2018.07.007>
- Mohriak, W., Nemčok, M., Enciso, G.: South Atlantic divergent margin evolution: Rift-border uplift and salt tectonics in the basins of SE Brazil: *Geol. Soc. Lond. Spec. Publ.* **294**, 365–398 (2008)
- Mohriak, W.: Birth and development of continental margin basins: Analogies from the South Atlantic, North Atlantic, and the Red Sea. *AAPG Search Discov.* (2014)
- Muniz, M.C., Bosence, D.W.J.: Lacustrine carbonate platforms: facies, cycles, and tectonosedimentary models for the presalt lagoa feia group (lower cretaceous), Campos basin, Brazil. *Am. Assoc. Petrol. Geol. Bull.* **102**(12), 2569–2597 (2018). <https://doi.org/10.1306/0511181620617087>
- Muniz, M.C.: Tectono-stratigraphic evolution of the Barremian-Aptian continental rift carbonates in southern Campos Basin, Brazil. Ph.D. thesis. Royal Holloway, University of London (2013)
- Oliveira, P.E.: Fósseis de Propiá e Jaboatão Estado De Sergipe: Serviço Geológico e Mineralógico. *Notas Preliminares e Estudos* **15**, 11–16 (1937)

- Oliveira, V.C.B., Silva, C.M.A., Borghi, L.F., Carvalho, I.S.: Lacustrine coquinas and hybrid deposits from rift phase: pre-Salt, lower Cretaceous, Campos Basin, Brazil. *J. South Am. Earth Sci.* **95**, 102254 (2019). <https://doi.org/10.1016/j.jsames.2019.102254>
- Olivito, J.P.R., Souza, F.J.: Depositional model of early Cretaceous lacustrine carbonate reservoirs of the Coqueiros Formation–northern Campos Basin, southeastern Brazil. *Mar. Petrol. Geol.* **111**, 414–439 (2020). <https://doi.org/10.1016/j.marpetgeo.2019.07.013>
- Otsuki, B., Takemoto, M., Fujibayashi, S., Neo, M., Kokubo, T., Nakamura, T.: Pore throat size and connectivity determine bone and tissue ingrowth into porous implants: three-dimensional micro-CT based structural analyses of porous bioactive titanium implants. *Biomaterials* (2006). <https://doi.org/10.1016/j.biomaterials.2006.08.013>
- Pal, A.K., Ravi, G., S., Ravi, K., Nair, A.M.: Pore scale image analysis for petrophysical modelling. *Micron* (2022). <https://doi.org/10.1016/j.micron.2021.103195>
- Pettijohn, F.J.: *Sedimentary Rocks*, 3rd edn. Harper and Row, New York (1957)
- Porto-Barros, J.P., Mendes, I.D., Dal'Bo, P.F.: Features of meteoric diagenesis in coquinas of Morro do Chaves Formation (Barremian-Aptian of Sergipe-Alagoas Basin). *Brazil. J. Geol.* **50**, e20190072–e20190081 (2020)
- Pudney, C.: Distance-ordered homotopic thinning: a skeletonization algorithm for 3D digital images. *Comput. vis. Image Underst.* **72**(3), 404–413 (1998). <https://doi.org/10.1006/cviu.1998.0680>
- Raouf, A., Nick, H.M., Hassanizadeh, S.M., Spiers, C.J.: PoreFlow: a complex pore-network model for simulation of reactive transport in variably saturated porous media. *J. Comput. Geosci.* (2013). <https://doi.org/10.1016/j.cageo.2013.08.005>
- Riguetti, A.L., Dal'Bo, P.F., Borghi, L., Mendes, M.: Bioclastic accumulation in a lake rift basin: the early cretaceous coquinas of the Sergipe-Alagoas basin, Brazil. *J. Sediment. Res.* **90**(2), 228–249 (2020). <https://doi.org/10.2110/jsr.2020.11>
- Sahimi, M.: *Flow and Transport in Porous Media and Fractured Rock: From Classical Methods to Modern Approaches*. Wiley, Germany (2012)
- Schäfer, W.: *Ecology and Paleoecology of Marine Environments*. The University of Chicago Press, Chicago (1972)
- Silva, P.N., Gonçalves, E.C., Rios, E.H., Muhammad, A., Moss, A., Pritchard, T., Glassborow, B., Plastino, A., Azeredo, R.B.V.: Automatic classification of carbonate rocks permeability from ^1H NMR relaxation data. *Expert Syst. Appl.* (2015). <https://doi.org/10.1016/j.eswa.2015.01.034>
- Skalinski, M., Kenter, J.A.M.: Carbonate petrophysical rock typing: integration geological attributes and petrophysical properties while linking with dynamic behavior. *Geol. Soc. Lond. Spec. Publ.* **406**(1), 229–259 (2015). <https://doi.org/10.1144/SP406.6>
- Souza, A. A.: Estudo de propriedades petrofísicas de rochas sedimentares por Ressonância Magnética Nuclear. 207 p. In: PhD thesis in Materials Science and Engineering, São Paulo University, (2012).
- Souza, A., Carneiro, G., Zielinski, L., Polinski, R., Schwartz, L., Hürlimann, M. D., Boyd, A., Rios, E. H., Santos B. C. C., Trevisan W. A., Machado, V. F., Azeredo, R. B. V. Permeability Prediction Improvement using 2D NMR Diffusion-T2 Maps. In: SPWLA 54th Annual Logging Symposium, New Orleans, Louisiana. (2013).
- Sun, H., Vega, S., Tao, G.: Analysis of heterogeneity and permeability anisotropy in carbonate rock samples using digital rock physics. *J. Petrol. Sci. Eng.* **156**, 419–429 (2017)
- Tavares, A.C., Borghi, L., Corbett, P., Nobre-Lopes, J., Câmara, R.: Facies and depositional environments for the coquinas of the Morro do Chaves Formation, Sergipe-Alagoas Basin, defined by taphonomic and compositional criteria. *Brazil. J. Geol.* **45**(3), 415–429 (2015)
- Thompson, D.L., Stilwell, J.D., Hall, M.: Lacustrine carbonate reservoirs from Early Cretaceous rift lakes of Western Gondwana: Pre-Salt coquinas of Brazil and West Africa. *Gondwana Res.* **28**(1), 26–51 (2015). <https://doi.org/10.1016/j.gr.2014.12.005>
- Tian, F., Wang, W., Liu, N.: Rock-type definition and pore characterization of tight carbonate rocks based on thin sections and MICP and NMR experiments. *Appl. Magn. Reson.* **49**, 631–652 (2018). <https://doi.org/10.1007/s00723-018-0993-2>
- Vasilyev, L., Raouf, A., Nordbotten, J.M.: Effect of mean network coordination number on dispersivity characteristics. *Transp. Porous Media* (2012). <https://doi.org/10.1007/s11242-012-0054-5>
- Wang, M., Xie, J., Guo, F., Zhou, Y., Yang, X., Meng, Z.: Determination of NMR T_2 cutoff and CT scanning for pore structure evaluation in mixed siliciclastic–carbonate rocks before and after acidification. *Energies* **13**, 1338 (2020a). <https://doi.org/10.3390/en13061338>
- Wang, L., Zhang, Y., Zhang, N., Zhao, C., Wu, W.: Pore structure characterization and permeability estimation with a modified multimodal Thomeer pore size distribution function for carbonate reservoirs. *J. Petrol. Sci. Eng.* (2020b). <https://doi.org/10.1016/j.petrol.2020.107426>
- Wentworth, C.K.: A scale of grade and class terms for clastic sediments. *J. Geol.* **30**, 377–392 (1922)

- Wildenschild, D., Sheppard, A.P.: X-ray imaging and analysis techniques for quantifying pore-scale structure and processes in subsurface porous medium systems. *Adv. Water Resour.* **51**(217–246), 246 (2013). <https://doi.org/10.1016/j.advwatres.2012.07.018>
- Yuan, Y., Rezaee, R.: Comparative porosity and pore structure assessment in Shales: measurement techniques, influencing factors and implications for reservoir characterization. *Energies* **12**, 2094 (2019). <https://doi.org/10.3390/en12112094>
- Zeng, J., Feng, X., Feng, S., Zhang, Y., Qiao, J., Yang, Z.: Influence of tight sandstone micro-nano pore-throat structures on petroleum accumulation: evidence from experimental simulation combining x-ray tomography. *J. Nanosci. Nanotechnol.* (2017). <https://doi.org/10.1166/jnn.2017.14514>
- Zhao, H., Ning, Z., Zhao, T., Zhang, R., Wang, Q.: Effects of mineralogy on petrophysical properties and permeability estimation of the Upper Triassic Yanchang tight oil sandstones in Ordos Basin, Northern China. *Fuel* (2016). <https://doi.org/10.1016/j.fuel.2016.08.096>
- Zhao, Z., Zhou, X., Qian, Q.: DQNN: Pore-scale variables-based digital permeability assessment of carbonates using quantum mechanism-based machine-learning. *Sci China Technol Sci.* **65**, 458–469 (2022). <https://doi.org/10.1007/s11431-021-1906-1>

Publisher's Note Springer Nature remains neutral with regard to jurisdictional claims in published maps and institutional affiliations.